Dalton Transactions

ROYAL SOCIETY OF CHEMISTRY

PAPER

View Article Online
View Journal | View Issue

Cite this: *Dalton Trans.*, 2025, **54**, 16356

Synthesising a series of promising ultraviolet nonlinear optical materials with the aid of the flexibility of isolated $[B_5O_{10}]$ groups

Yixin Song, Hongwei Yu, * Hongping Wu, * Zhanggui Hu, Jiyang Wang and Yicheng Wu

Received 15th August 2025,
Accepted 7th October 2025

DOI: 10.1039/d5dt01944c

rsc.li/dalton

Eight new compounds, namely $K_7MgSc_2(B_5O_{10})_3$, $K_7Sr_{0.34}Sc_{2.44}(B_5O_{10})_3$, $K_6Li_{0.94}BaY_{2.02}(B_5O_{10})_3$, $K_6NaBaY_2(B_5O_{10})_3$, $Rb_{5.3}Na_{3.7}Y_2(B_5O_{10})_3$, $Rb_6Na_{1.5}Y_{2.5}(B_5O_{10})_3$, $K_6Na_{1.82}Y_{2.18}(B_5O_{10})_3$, and $K_7Mg_{0.88}Zn_{0.12}Y_2(B_5O_{10})_3$, were successfully synthesized with the aid of the flexibility of isolated anion groups. All the compounds crystallize in the non-centrosymmetric (NCS) space group *R*32. Their structures feature a zero-dimensional configuration composed of isolated $[B_5O_{10}]$ groups, which are connected by an $[MO_6]$-based octahedron, forming a three-dimensional framework with tunnels filled by the other cations. The compounds show an appropriate second harmonic generation (SHG) response, comparable to that of commercial KH_2PO_4 (KDP), and a short ultraviolet (UV) cut-off edge (<190 nm), achieving optimal balance between the two critical parameters for nonlinear optical (NLO) applications in the UV region. Additionally, for a deeper investigation of the structural flexibility, a comparison was carried out in $A_7MRE_2(B_5O_{10})_3$ (A = alkali metal, M = divalent element, and RE = rare earth metal) structures. The fascinating results indicate that the single point link between the M cation-centered octahedron and isolated $[B_5O_{10}]$ groups increases the structural flexibility and adjustability to accommodate varied cations, providing the foundations for the design of novel compositions.

Introduction

Ultraviolet (UV) nonlinear optical (NLO) materials, which can halve the wavelength of light (or double the frequency) through second-harmonic generation (SHG), have significant applications in material micromachining, laser medical treatment, and photolithography.[1–6] In the past several decades, numerous NLO materials, including borates, phosphates, carbonates, and nitrates, have been explored for promising UV and deep-ultraviolet (DUV) applications.[7–12] Among these, borates have emerged as preferred candidates due to their distinctive structures composed of π-conjugated $[BO_3]$ and $[BO_4]$ units, which confer performance advantages, such as a short UV cut-off edge, large SHG response and/or suitable birefringence.[13–15] Notable examples include β-BaB_2O_4 (β-BBO),[16] LiB_3O_5 (LBO),[17] $CsLiB_6O_{10}$ (CLBO),[18] and $KBe_2BO_3F_2$ (KBBF),[19] all of which display wide transparency windows extending into the DUV region and a large SHG coefficient (comparable to or larger than that of KH_2PO_4 (KDP, $d_{36} \approx 0.39$ pm V^{-1})). KBBF is regarded as the sole material that is amenable to the direct generation of coherent light below 200 nm.[20] However, its layering tendency in single-crystal growth and the toxicity of beryllium oxide severely limit its potential applications.[21] Consequently, the effective design and synthesis of novel UV/DUV NLO materials have emerged as essential goals in research.

In crystal engineering, an efficient approach for discovering novel UV NLO materials involves using classical structures as templates or modifying them.[22–29] For example, based on the structural framework of KBBF, several borates, including $NH_4B_4O_6F$,[30] $CsZn_2B_3O_7$,[31] and $BaAlBO_3F_2$,[32] have been developed. Among them, $NH_4B_4O_6F$ shows excellent NLO properties including a large SHG response (3× KDP), adequate birefringence (0.117@1064 nm), and a DUV cut-off edge (156 nm). Moreover, through combining diverse host and guest functional units within the gaudefroyite family, many new compounds with honeycomb frameworks of different types of chains, such as $Ba_3Sr_4(BO_3)_3F_5$,[33] $Ba_3La_4O_4(BO_3)_3X$ (X = F, Cl, and Br), and $Sr_5La(BO_3)_4X$ (X = Cl, Br),[34] were reported. Based on the above analysis, it is not hard to notice that the selection of a suitable framework is conducive to designing new NLO materials.

Recent attention has turned to the $A_7MRE_2(B_5O_{10})_3$ family (A = alkali metal, M = divalent element, and RE = rare earth

State Key Laboratory of Crystal Materials, Tianjin Key Laboratory of Functional Crystal Materials, Institute of Functional Crystals, Tianjin University of Technology, Tianjin 300384, China. E-mail: yuhw@email.tjut.edu.cn, wuhp2022@163.com

metal).[35] The structural adaptability of these compounds—achieved by substituting cations with different electronic configurations at the A, M, and RE sites—enables the design of non-centrosymmetric (NCS) structures while preserving the stable $[B_5O_{10}]$ framework. This suggests that elemental substitution within this family could be a promising strategy for developing NLO materials. The element selection critically influences optical performance. Preference is given to alkali, alkaline earth or rare-earth cations lacking d–d and f–f electronic transitions for applications in the short-wavelength UV region, as they help extend transparency into the UV/DUV range.[36–38] Additionally, distorted polyhedra formed by rare-earth cations coordinated with oxygen atoms exhibit high hyperpolarizability, enhancing the SHG effect in NCS compounds.[39,40] By incorporating these features, materials in this series achieve a balance between short UV cut-off edges and large SHG responses.[35]

Inspired by this approach, we incorporated a range of alkali, alkaline earth, and rare-earth cations into $A_7MRE_2(B_5O_{10})_3$, and eight new NCS compounds, $K_7MgSc_2(B_5O_{10})_3$, $K_7Sr_{0.34}Sc_{2.44}(B_5O_{10})_3$, $K_6Li_{0.94}BaY_{2.02}(B_5O_{10})_3$, $K_6NaBaY_2(B_5O_{10})_3$, $K_7Mg_{0.88}Zn_{0.12}Y_2(B_5O_{10})_3$, $Rb_6Na_{1.5}Y_{2.5}(B_5O_{10})_3$, $K_6Na_{1.82}Y_{2.18}(B_5O_{10})_3$, and $Rb_{5.3}Na_{3.7}Y_2(B_5O_{10})_3$, were successfully synthesized. Notably, as anticipated, the rigid $[MO_6]$ octahedra form a triangular framework that immobilizes the flexible $[B_5O_{10}]$ anionic groups, while the remaining cations fill the framework channels. Consequently, the structural configuration remains largely unaffected by the filling cations, ensuring the stability of the NCS configuration. These findings provide valuable insights for the design of NCS materials. The property measurements reveal promising optical characteristics, including a short UV cut-off edge (<190 nm) and an appropriate SHG response (0.96–1.33× KDP). Herein, we will present their crystal structures, functional properties, and theoretical calculations.

Results and discussion

Crystallographic analysis indicates that all eight compounds crystallize in the trigonal space group *R*32 (No. 155). The compounds are isomorphic, and as such, $K_7MgSc_2(B_5O_{10})_3$, $K_7Mg_{0.88}Zn_{0.12}Y_2(B_5O_{10})_3$, and $Rb_6Na_{1.5}Y_{2.5}(B_5O_{10})_3$ were chosen as representatives for detailed characterization. Solid-state reaction methods were employed to prepare polycrystalline samples of $K_7MgSc_2(B_5O_{10})_3$, $K_7Mg_{0.88}Zn_{0.12}Y_2(B_5O_{10})_3$, and $Rb_6Na_{1.5}Y_{2.5}(B_5O_{10})_3$, and their phase purity was checked by powder X-ray diffraction (PXRD) analysis (Fig. S1). TG-DSC was utilized to assess the thermal stabilities of $K_7MgSc_2(B_5O_{10})_3$, $K_7Mg_{0.88}Zn_{0.12}Y_2(B_5O_{10})_3$, and $Rb_6Na_{1.5}Y_{2.5}(B_5O_{10})_3$. The heating DSC curves display endothermic peaks at 884, 867, and 845 °C for $K_7MgSc_2(B_5O_{10})_3$, $K_7Mg_{0.88}Zn_{0.12}Y_2(B_5O_{10})_3$, and $Rb_6Na_{1.5}Y_{2.5}(B_5O_{10})_3$, respectively, while no reduction in weight is observed in the corresponding TG curves over the temperature range (Fig. S2), which indicates excellent thermal stability of the compounds. Furthermore, the PXRD patterns of melted $K_7MgSc_2(B_5O_{10})_3$, $K_7Mg_{0.88}Zn_{0.12}Y_2(B_5O_{10})_3$, and $Rb_6Na_{1.5}Y_{2.5}(B_5O_{10})_3$ vary from the calculated ones (Fig. S3), which shows their incongruent melting.

$K_7MgSc_2(B_5O_{10})_3$ is selected as a representative to elucidate the structural characteristics in detail. In the asymmetric unit of $K_7MgSc_2(B_5O_{10})_3$, there are three crystallographically unique K atoms, one Mg atom, one Sc atom, three B atoms, and five O atoms. As shown in Fig. 1, the B atoms exhibit two distinct coordination geometries, namely, $[BO_3]$ coplanar triangles and $[BO_4]$ tetrahedra, four $[BO_3]$ triangles and one $[BO_4]$ tetrahedron further connected by sharing a vertex O atom to form isolated $[B_5O_{10}]$ groups (Fig. 1a). The Sc atoms are coordinated by six O atoms to form $[ScO_6]$, and the discrete $[ScO_6]$ octahedra are further connected to the isolated $[B_5O_{10}]$ groups by sharing oxygen atoms to form a complex three-dimensional (3D) framework structure (Fig. 1b). The low-valence K^+ and Mg^{2+} cations are located in the cavities to maintain charge balance (Fig. 1d).

In the B–O anionic units, the B–O distances range from 1.323(9) to 1.407(9) Å for $[BO_3]$ triangles and from 1.461(9) to 1.464(9) Å for tetrahedral $[BO_4]$. The Mg–O distances are equal to 2.113(4) Å, while the Sc–O and K–O distances are in the ranges of 2.056(5)–2.195(5) Å and 2.636(5)–3.163(6) Å, respectively. Clearly, all these bond distances are consistent with those in other related compounds.[41] Furthermore, according to the Brown formula, the bond valence sum (BVS) analysis results in values of 1.08–1.39 for K^+, 1.94 for Mg^{2+}, 2.76 for Sc^{3+}, 3.00–3.05 for B^{3+}, and 1.8–2.23 for O^{2-} (Table S2). Each of these aligns with the expected oxidation states.[42]

Currently, there are 45 known compounds in the $A_7MRE_2(B_5O_{10})_3$ family including the compounds obtained in this work.[42–60] Interestingly, the compounds in the family, except $Rb_6LiCaY_2(B_5O_{10})_3$ (space group $C222_1$),[43] all crystallize in the *R*32 space group. According to the difference in substitution positions, we divided them into three sites: A, M, and RE. The A site is mainly composed of monovalent cations (Li, Na, K, Rb, *etc.*), the M site is composed of divalent cations (Mg, Ca, Zn, Cd, *etc.*), and the RE site is composed of rare earth elements (Sc, Y, Gd, Lu, *etc.*) (Fig. S4).

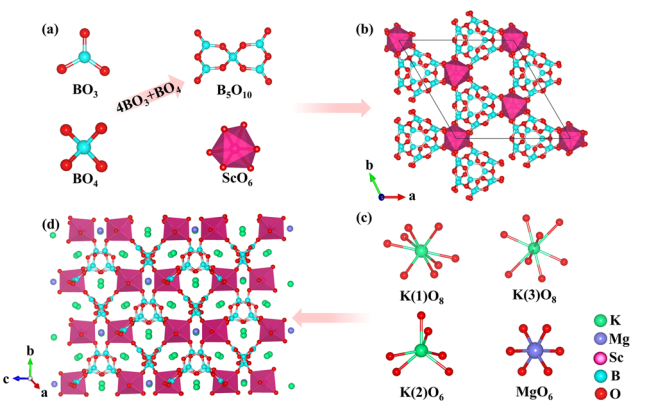

Fig. 1 (a) BO_3, BO_4, B_5O_{10}, and YO_6 groups; (b) 3D structure formed by YO_6 and B_5O_{10} groups; (c) KO_8, KO_6, and MgO_6 groups; and (d) the whole crystal structure of $K_7MgSc_2(B_5O_{10})_3$.

First, for the A site, a monovalent alkali metal substitution is appropriate. When equivalent substitution occurs with the A-site cations and the radius difference of the substituted ions is less than 0.5 Å, the structural framework in the space group *R*32 can remain. Conversely, a radius difference exceeding 0.5 Å leads to instability of the structural framework, thus inducing symmetry change (Fig. S5). For instance, compounds $Rb_6LiCaY_2(B_5O_{10})_3$ and $Rb_6NaCaY_2(B_5O_{10})_3$ (space group: *R*32) share similar molecular formulas, while exhibiting marked structural differences attributed to the Na^+ substitution with Li^+. For one thing, the $[B_5O_{10}]$ units in $Rb_6NaCaY_2(B_5O_{10})_3$ form a six-membered ring structure, and these six-membered rings are connected to each other to form a honeycomb B–O framework (Fig. S6a), while the $[B_5O_{10}]$ units in $Rb_6LiCaY_2(B_5O_{10})_3$ form a curved quadrilateral (Fig. S6b). For another thing, the difference in cation sizes is also a significant factor. In the structure of $Rb_6NaCaY_2(B_5O_{10})_3$, Na^+ is six-coordinated with a radius of 1.16 Å, exhibiting identical Na–O distances of 2.462(6) Å (Fig. S6c), while in $Rb_6LiCaY_2(B_5O_{10})_3$, the six-coordinated Li^+ radius is 0.9 Å and Li–O distances range from 2.019(9) to 2.425(11) Å (Fig. S6d). The radius difference between Li^+ and Rb^+ is greater than 0.5 Å. This means

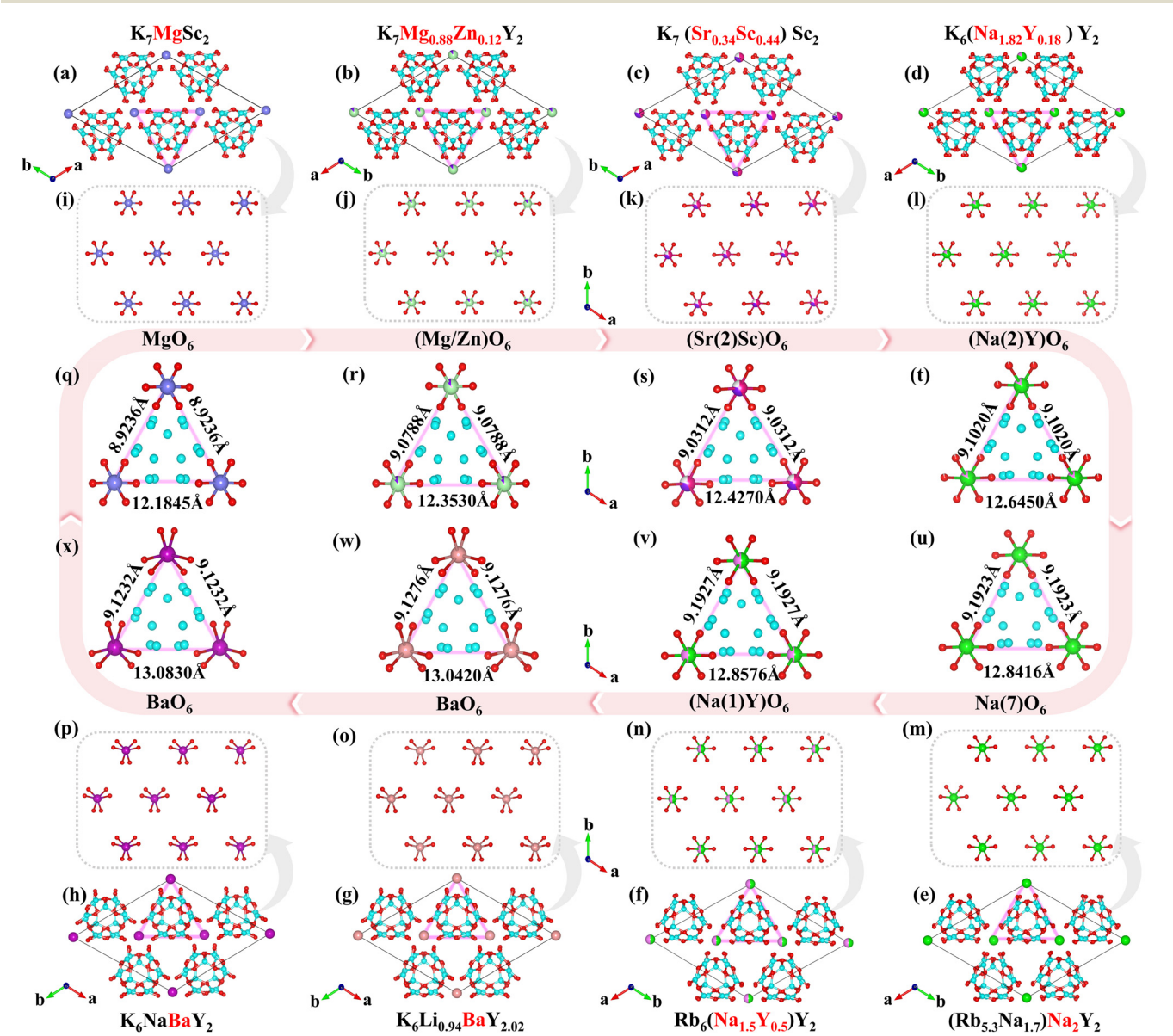

Fig. 2 Structures of (a) $K_7MgSc_2(B_5O_{10})_3$, (b) $K_7Mg_{0.88}Zn_{0.12}Y_2(B_5O_{10})_3$, (c) $K_7Sr_{0.34}Sc_{2.44}(B_5O_{10})_3$, (d) $K_6Na_{1.82}Y_{2.18}(B_5O_{10})_3$, (e) $Rb_{5.3}Na_{3.7}Y_2(B_5O_{10})_3$, (f) $Rb_6Na_{1.5}Y_{2.5}(B_5O_{10})_3$, (g) $K_6Li_{0.94}BaY_{2.02}(B_5O_{10})_3$, and (h) $K_6NaBaY_2(B_5O_{10})_3$; the arrangement of the zero-dimensional $[MO_6]$ octahedron in (i) $K_7MgSc_2(B_5O_{10})_3$, (j) $K_7Mg_{0.88}Zn_{0.12}Y_2(B_5O_{10})_3$, (k) $K_7Sr_{0.34}Sc_{2.44}(B_5O_{10})_3$, (l) $K_6Na_{1.82}Y_{2.18}(B_5O_{10})_3$, (m) $Rb_{5.3}Na_{3.7}Y_2(B_5O_{10})_3$, (n) $Rb_6Na_{1.5}Y_{2.5}(B_5O_{10})_3$, (o) $K_6Li_{0.94}BaY_{2.02}(B_5O_{10})_3$, and (p) $K_6NaBaY_2(B_5O_{10})_3$; and the $M(B_5O_{10})_3$ triangular open framework composed of the $[MO_6]$ octahedron and $[B_5O_{10}]$ groups in (q) $K_7MgSc_2(B_5O_{10})_3$, (r) $K_7Mg_{0.88}Zn_{0.12}Y_2(B_5O_{10})_3$, (s) $K_7Sr_{0.34}Sc_{2.44}(B_5O_{10})_3$, (t) $K_6Na_{1.82}Y_{2.18}(B_5O_{10})_3$, (u) $Rb_{5.3}Na_{3.7}Y_2(B_5O_{10})_3$, (v) $Rb_6Na_{1.5}Y_{2.5}(B_5O_{10})_3$, (w) $K_6Li_{0.94}BaY_{2.02}(B_5O_{10})_3$, and (x) $K_6NaBaY_2(B_5O_{10})_3$.

that when Na^+ is replaced by the Li^+ cation, the larger radius difference results in a broken threefold rotational axis of $[NaO_6]$ in $Rb_6NaCaY_2(B_5O_{10})_3$, and thus, $Rb_6LiCaY_2(B_5O_{10})_3$ crystallizes in the lower symmetric space group $C222_1$.

Second, for the M site, the distribution of the atoms will be slightly different when the atoms with different valences are substituted at the M-site. According to bond valence theory, we obtained a series of compounds in this work. As shown in Fig. 2, all structures contain a triangular open framework $M(B_5O_{10})_3$ composed of an $[MO_6]$ octahedron and $[B_5O_{10}]$ groups with co-point connection. With the change of the atomic radius from Mg to Mg/Zn, Sr/Sc, Na/Y, Na, and Ba, which does not induce a change of the space group, the $M(B_5O_{10})_3$ frame tunnel can scale up and down with the variation of the atomic radius and chemical bond. The flexible configuration further enables the co-existence of $[B_{15}O_{30}]$ clusters in all of the title compounds.

Third, for the RE site, at present, the elements Sc, Y, Gd, and Lu whose d orbitals are fully occupied are mainly studied. Because these coordination environments are similar, there is no difference in the atomic distribution in the structure (Fig. S7), which has no effect on the structural configuration. Based on the above analysis, we can conclude that in the $A_7MRE_2(B_5O_{10})_3$ family, when the A-site atoms are equivalently replaced, an atomic radius difference greater than 0.5 Å will affect the structural configuration, causing symmetry change. The M and RE sites have an insignificant effect on the structural configuration.

The IR spectra of $K_7MgSc_2(B_5O_{10})_3$, $K_7Mg_{0.88}Zn_{0.12}Y_2(B_5O_{10})_3$, and $Rb_6Na_{1.5}Y_{2.5}(B_5O_{10})_3$ are shown in Fig. 3a. Clearly, all reported compounds show similar IR absorption spectra, with the absorption peaks located at 1180–1370 and 917–944 cm^{-1} attributed to asymmetric stretching and symmetric stretching vibrations of the $[BO_3]$ groups, respectively.[50,51] The asymmetric stretching vibrations of the $[BO_4]$ units were observed at 1026–1035 cm^{-1}, whereas the symmetric stretching vibration of this unit was observed at 722–785 cm^{-1}.[56,57] Meanwhile, the absorption peaks appearing at 608–622 cm^{-1} are ascribed to the bending vibrations of both $[BO_3]$ and $[BO_4]$ groups. These characteristic peaks confirm the existence of the $[BO_3]$ and $[BO_4]$ groups in these structures, consistent with the previously reported results,[40] further supporting the rationality of structural analysis. Additionally, the UV-vis-NIR diffuse-reflectance spectra recorded for the three compounds are shown in Fig. 3b. Each of these compounds has a wide transmission from 190 to 2000 nm, and their reflectance is still above 40% even at 190 nm, which is comparable to that in other compounds in the $A_7MRE_2(B_5O_{10})_3$ family, such as $Rb_6NaCaY_2(B_5O_{10})_3$ (185 nm), $K_7SrY_2(B_5O_{10})_3$ (<190 nm), $K_7BaSc_2(B_5O_{10})_3$ (190 nm), *etc.*, indicating that they all have the potential as DUV NLO materials.

Given that these compounds are NCS, we evaluated the NLO properties of $K_7MgSc_2(B_5O_{10})_3$, $K_7Mg_{0.88}Zn_{0.12}Y_2(B_5O_{10})_3$, and $Rb_6Na_{1.5}Y_{2.5}(B_5O_{10})_3$. The SHG intensity increases with the increase of particle size in the range of 25–250 μm, which

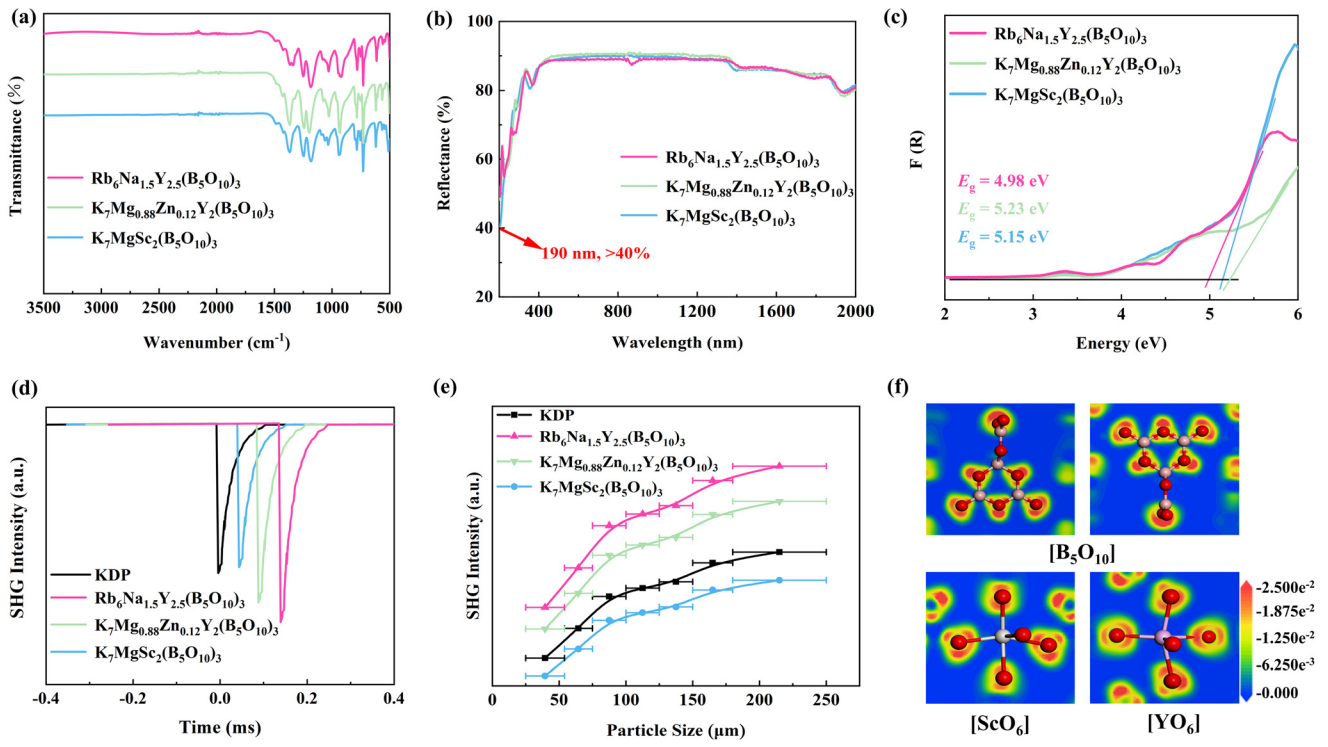

Fig. 3 (a) IR spectra; (b) UV-vis-NIR diffuse reflectance spectra; (c) band gap determination; (d and e) powder SHG signals under pumping at 1064 nm (in panel (e), the curves are drawn to guide the eye, not to represent a fit to the data in panel (d)); and (f) ELF iso-surfaces of oxygen around B and RE (RE = Sc and Y) atoms.

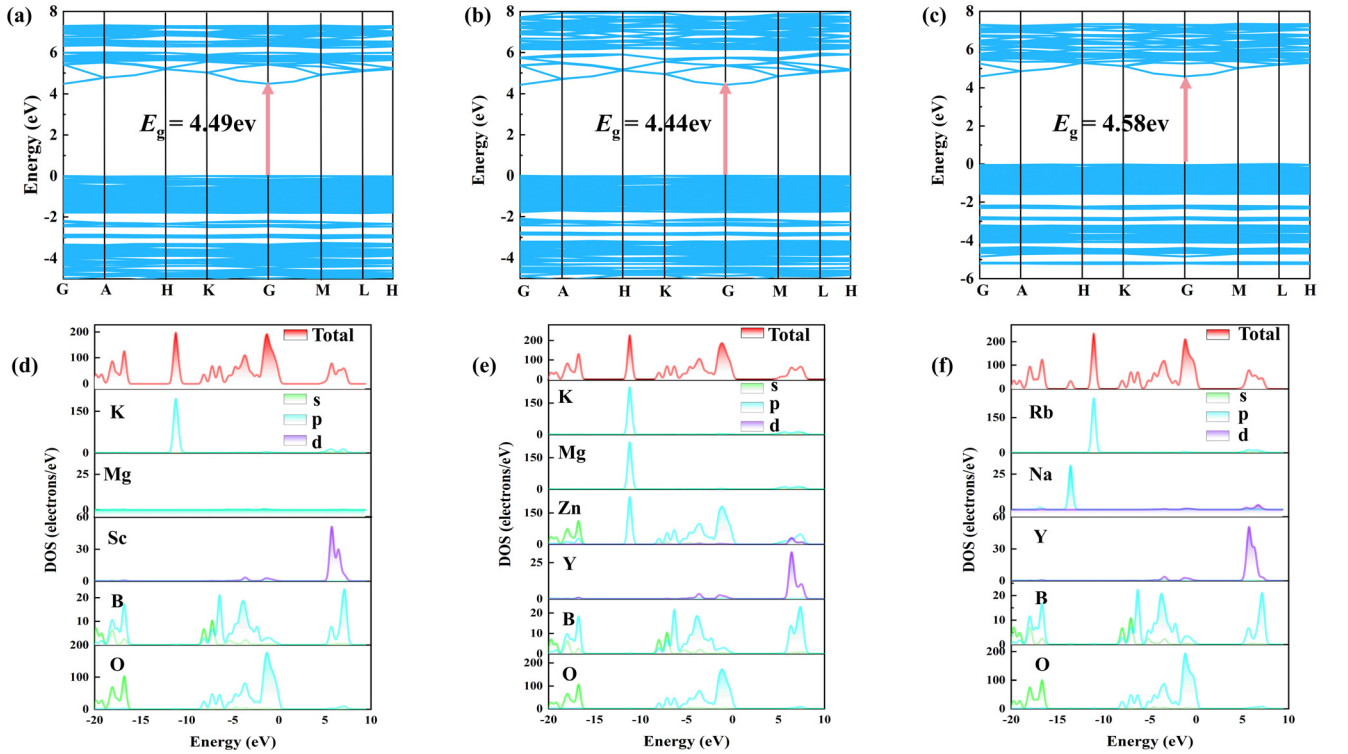

Fig. 4 Electronic band structures of (a) $K_7MgSc_2(B_5O_{10})_3$, (b) $K_7Mg_{0.88}Zn_{0.12}Y_2(B_5O_{10})_3$, and (c) $Rb_6Na_{1.5}Y_{2.5}(B_5O_{10})_3$. Total and partial densities of states of (d) $K_7MgSc_2(B_5O_{10})_3$, (e) $K_7Mg_{0.88}Zn_{0.12}Y_2(B_5O_{10})_3$, and (f) $Rb_6Na_{1.5}Y_{2.5}(B_5O_{10})_3$.

indicates that all three materials are phase matchable (PM) (Fig. 3e). The comparison of the SHG signals produced by $K_7MgSc_2(B_5O_{10})_3$, $K_7Mg_{0.88}Zn_{0.12}Y_2(B_5O_{10})_3$, $Rb_6Na_{1.5}Y_{2.5}(B_5O_{10})_3$ and KDP powder samples with the particle sizes in the same range (180–250 μm) reveals that the borates exhibit significant SHG responses equal to ~0.96, 1.20, and 1.33× KDP (Fig. 3d), respectively.

In order to study the difference in SHG response, we calculated the number density of NLO active groups of the compounds. From $K_7MgSc_2(B_5O_{10})_3$ (0.0127 $Å^{-3}$) to $K_7Mg_{0.88}Zn_{0.12}Y_2(B_5O_{10})_3$ (0.0130 $Å^{-3}$) and $Rb_6Na_{1.5}Y_{2.5}(B_5O_{10})_3$ (0.0142 $Å^{-3}$), the number density of NLO active groups shows an increasing trend, which is consistent with their order of SHG intensity. Furthermore, we compared the number density value of NLO active groups of $Na_4Ga_3B_4O_{12}(OH)$[61] (0.1× KDP, number density: 0.0125 $Å^{-3}$) with a similar borate framework, and it also falls on the trend line, thereby consolidating the above conclusion. In addition, from the electron localization function (ELF), one can see the elliptical and clover-shaped asymmetric electron density arrangements around the oxygen atoms in $[B_5O_{10}]$ and $[REO_6]$ groups, which indicates that they provide a positive contribution to the SHG response (Fig. 3f).

To further understand the structure–performance relationship, we calculated the electronic structure and optical properties of the three compounds. The results show that they all exhibit direct band gaps of 4.49 ($K_7MgSc_2(B_5O_{10})_3$), 4.44 eV ($K_7Mg_{0.88}Zn_{0.12}Y_2(B_5O_{10})_3$), and 4.58 eV ($Rb_6Na_{1.5}Y_{2.5}(B_5O_{10})_3$) (Fig. 4a–c). The calculated smaller band gap can be attributed to the discontinuity in the correlation exchange energy. Furthermore, based on the total density of states and partial density of states, it can be seen that the top valence bands primarily consist of B 2p and O 2p orbitals, whereas the bottom of the conduction bands is mainly derived from the B 2p and RE 4d orbitals (Fig. 4d–f). These findings indicate that the synergistic effect between the RE–O and B–O groups is the main factor governing the optical properties.

Conclusions

In summary, eight NCS rare-earth borates, $K_7MgSc_2(B_5O_{10})_3$, $K_7Sr_{0.34}Sc_{2.44}(B_5O_{10})_3$, $K_6Li_{0.94}BaY_2(B_5O_{10})_3$, $K_6NaBaY_2(B_5O_{10})_3$, $K_7Mg_{0.88}Zn_{0.12}Y_2(B_5O_{10})_3$, $Rb_6Na_{1.5}Y_{2.5}(B_5O_{10})_3$, $K_6Na_{1.82}Y_{2.18}(B_5O_{10})_3$, and $Rb_{5.3}Na_{3.7}Y_2(B_5O_{10})_3$, were successfully synthesized *via* a high-temperature solid-state reaction method. Structural analysis shows that the triangular open framework $M(B_5O_{10})_3$, which is formed by the single point connection of an $[MO_6]$ octahedron and $[B_5O_{10}]$ groups, provides great flexibility and adjustability in the replacement of M-site cations. In addition, $K_7MgSc_2(B_5O_{10})_3$, $K_7Mg_{0.88}Zn_{0.12}Y_2(B_5O_{10})_3$, and $Rb_6Na_{1.5}Y_{2.5}(B_5O_{10})_3$ exhibit a short UV cut-off edge (<190 nm) and good PM SHG response (0.96–1.33 × KDP). The investigation into the structure–performance relationship shows that

the synergistic effect of $[B_5O_{10}]$ and $[REO_6]$ building units provides the main contribution to their NLO responses.

Author contributions

Yixin Song: conceptualization, writing – original draft, and writing – review & editing; Hongwei Yu: funding acquisition, project administration, supervision, and validation; Hongping Wu: software, supervision, and writing – review & editing; Zhanggui Hu: project administration; Jiyang Wang: supervision; Yicheng Wu: project administration and resources.

Conflicts of interest

There are no conflicts to declare.

Data availability

The data supporting this article have been included as part of the supplementary information (SI). Supplementary information: experimental details, crystallographic data, atomic coordinates, displacement parameters and BVS, selected bond distances and angles, PXRD, TG-DSC, and the collation and comparison of $A_7MRE_2(B_5O_{10})_3$ family compounds. See DOI: https://doi.org/10.1039/d5dt01944c.

CCDC 2475240 ($K_7Mg_{0.88}Zn_{0.12}Y_2(B_5O_{10})_3$), 2475241 ($Rb_{5.3}Na_{3.7}Y_2(B_5O_{10})_3$), 2475242 ($Rb_6Na_{1.5}Y_{2.5}(B_5O_{10})_3$), 2475243 ($K_6Na_{1.82}Y_{2.18}(B_5O_{10})_3$), 2475244 ($K_7Sr_{0.34}Sc_{2.44}(B_5O_{10})_3$), 2475245 ($K_6NaBaY_2(B_5O_{10})_3$), 2475246 ($K_7MgSc_2(B_5O_{10})_3$), and 2475247 ($K_6Li_{0.94}BaY_2(B_5O_{10})_3$) contain the supplementary crystallographic data for this paper.[62a–h]

Acknowledgements

This work was supported by the National Natural Science Foundation of China (Grant No. 52322202 and 52172006) and the Tianjin Natural Science Foundation (Grant No. 21JCJQJC00090).

References

1 M. Mutailipu, K. R. Poeppelmeier and S. Pan, *Chem. Rev.*, 2020, **121**, 1130–1202.
2 H. Wu, Z. Wei, Z. Hu, J. Wang, Y. Wu and H. Yu, *Angew. Chem., Int. Ed.*, 2024, **63**, e202406318.
3 Z. Yan, J. Fan, S. Pan and M. Zhang, *Chem. Soc. Rev.*, 2024, **53**, 6568–6599.
4 G. Peng, C. Lin, H. Fan, K. Chen, B. Li, G. Zhang and N. Ye, *Angew. Chem., Int. Ed.*, 2021, **60**, 17415–17418.
5 F. Bu, H. Wu, Z. Hu, J. Wang, Y. Wu and H. Yu, *Adv. Funct. Mater.*, 2024, **35**, 202414666.
6 H. Liu, H. Wu, Z. Hu, J. Wang, Y. Wu and H. Yu, *J. Am. Chem. Soc.*, 2023, **145**, 12691–12700.
7 H. Yu, H. Wu, S. Pan, Z. Yang, X. Hou, X. Su, Q. Jing, K. R. Poeppelmeier and J. M. Rondinelli, *J. Am. Chem. Soc.*, 2014, **136**, 1264–1267.
8 Y. Yang, S. Huang and S. Pan, *J. Mater. Chem. C*, 2022, **10**, 11232–11238.
9 J. Chen, L. Xiong, L. Chen and L. M. Wu, *J. Am. Chem. Soc.*, 2018, **140**, 14082–14086.
10 J. X. Zhang, Q. G. Yue, S. H. Zhou, X. T. Wu, H. Lin and Q. L. Zhu, *Angew. Chem., Int. Ed.*, 2024, **63**, e202413276.
11 Y. Deng, L. Huang, X. Dong, L. Wang, K. M. Ok, H. Zeng, Z. Lin and G. Zou, *Angew. Chem., Int. Ed.*, 2020, **59**, 21151–21156.
12 Y. Tian, W. Zeng, X. Dong, L. Huang, Y. Zhou, H. Zeng, Z. Lin and G. Zou, *Angew. Chem., Int. Ed.*, 2024, **63**, e202409093.
13 Y. Wu, C. Cui, Z. Wang, J. Li, J. Han, M. Mutailipu and S. Pan, *Adv. Mater.*, 2025, 2505930.
14 H. Liu, X. Zhai, X. Li, H. Wu, Z. Hu, J. Wang, Y. Wu and H. Yu, *Angew. Chem., Int. Ed.*, 2025, **64**, e202502252.
15 C. Chen, Y. Wu and R. Li, *Mater. Nonlinear Opt.*, 1991, **455**, 360–379.
16 C. T. Chen, B. C. Wu, A. D. Jiang and G. M. You, *Sci. Sin., Ser. B*, 1985, **28**, 235–243.
17 C. T. Chen, Y. C. Wu, A. D. Jiang, B. C. Wu, G. M. You, R. K. Li and S. J. Lin, *J. Opt. Soc. Am. B*, 1989, **6**, 616–621.
18 Y. Mori, I. Kuroda, S. Nakajima, T. Sasaki and S. Nakai, *Appl. Phys. Lett.*, 1995, **67**, 1818–1820.
19 C. T. Chen, G. L. Wang, X. Y. Wang and Z. Y. Xu, *Appl. Phys. B*, 2009, **97**, 9–25.
20 C. Chen, Z. Xu, D. Deng, J. Zhang, G. K. L. Wong, B. Wu, N. Ye and D. Tang, *Appl. Phys. Lett.*, 1996, **68**, 2930–2932.
21 B. Wu, D. Tang, N. Ye and C. Chen, *Opt. Mater.*, 1996, **5**, 105–109.
22 G. Yang, P. Gong, Z. Lin and N. Ye, *Chem. Mater.*, 2016, **28**, 9122–9131.
23 S. Wang and N. Ye, *J. Am. Chem. Soc.*, 2011, **133**, 11458–11461.
24 M. Mutailipu, M. Zhang, H. Wu, Z. Yang, Y. Shen, J. Sun and S. Pan, *Nat. Commun.*, 2018, **9**, 3089.
25 K. M. Ok, *Acc. Chem. Res.*, 2016, **49**, 2774–2785.
26 V. V. Atuchin, B. G. Bazarov, T. A. Gavrilova, V. G. Grossman, M. S. Molokeev and Z. G. Bazarova, *J. Alloys Compd.*, 2012, **515**, 119–122.
27 V. V. Atuchin, A. K. Subanakov, A. S. Aleksandrovsky, B. G. Bazarov, J. G. Bazarova, T. A. Gavrilova, A. S. Krylov, M. S. Molokeev, A. S. Oreshonkov and S. Y. Stefanovich, *Mater. Des.*, 2018, **140**, 488–494.
28 X. Dong, L. Huang, C. Hu, H. Zeng, Z. Lin, X. Wang, K. M. Ok and G. Zou, *Angew. Chem., Int. Ed.*, 2019, **58**, 6528–6534.
29 X. Dong, L. Huang and G. Zou, *Acc. Chem. Res.*, 2025, **58**, 150–162.
30 G. Shi, Y. Wang, F. Zhang, B. Zhang, Z. Yang, X. Hou, S. Pan and K. R. Poeppelmeier, *J. Am. Chem. Soc.*, 2017, **139**, 10645–10648.

31 S. Zhao, J. Zhang, S. Q. Zhang, Z. Sun, Z. Lin, Y. Wu, M. Hong and J. Luo, *Inorg. Chem.*, 2014, **53**, 2521–2527.
32 C. Chen, D. Dou, Y. Bai, B. Zhang and Y. Wang, *Inorg. Chem. Front.*, 2024, **11**, 6020–6027.
33 G. Zhang, Z. Liu, J. Zhang, F. Fan, Y. Liu and P. Fu, *Cryst. Growth Des.*, 2009, **9**, 3137–3141.
34 B. Yuan, H. Wu, Z. Hu, J. Wang, Y. Wu and H. Yu, *Chem. Mater.*, 2022, **34**, 8004–8012.
35 N. He, P. Gong and Z. Lin, *J. Synth. Cryst.*, 2022, **51**, 1598–1607.
36 Y. V. Seryotkin, V. V. Bakakin, A. E. Kokh, N. G. Kononova, T. N. Svetlyakova, K. A. Kokh and T. N. Drebushchak, *J. Solid State Chem.*, 2010, **183**, 1200–1204.
37 G. Sun, X. Qi, H. Wu, Z. Hu, J. Wang and Y. Wu, *Inorg. Chem. Front.*, 2024, **11**, 3245–3253.
38 J. Chen, J. Zhang, A. Zhu and X. Huang, *New J. Chem.*, 2022, **46**, 19629–19632.
39 R. Liu, H. Wu, H. Yu, Z. Hu, J. Wang and Y. Wu, *Chem. Mater.*, 2021, **33**, 4240–4246.
40 M. Liu, X. Kong, S. Li, N. Ye, Z. Hu, Y. Wu and C. Li, *Chem. Commun.*, 2025, **61**, 3155–3158.
41 Z. Xie, M. Mutailipu, G. He, G. Han, Y. Wang, Z. Yang, M. Zhang and S. Pan, *Chem. Mater.*, 2018, **30**, 2414–2423.
42 N. E. Brese and M. O'Keeffe, *Acta Crystallogr.*, 1991, **47**, 192–197.
43 C. Wu, Y. Dang, J. Chen, X. Hou and H. Shi, *Cryst. Growth Des.*, 2023, **23**, 6885–6893.
44 S. Zhao, G. Zhang, J. Yao and Y. Wu, *CrystEngComm*, 2012, **14**, 5209–5214.
45 S. Li, W. Li, X. Li, G. Yang, N. Ye, Z. Hu, Y. Wu and C. Li, *Chem. Sci.*, 2024, **15**, 8959–8965.
46 W. Liu, M. H. Lee, R. Guo and J. Yao, *Dalton Trans.*, 2023, **52**, 3344–3350.
47 X. Kong, J. Chai, H. Zhao, N. Ye, Z. Hu, Y. Wu and C. Li, *Inorg. Chem. Front.*, 2025, **12**, 630–636.
48 J. Feng, X. Xu, C. L. Hu and J. G. Mao, *Inorg. Chem.*, 2019, **58**, 2833–2839.
49 X. Gao, Q. Liu, Z. Yang, J. Han and S. Pan, *Inorg. Chem.*, 2025, **64**, 5821–5826.
50 Y. Li, F. Liang, H. Song, W. Liu, Z. Lin, G. Zhang and Y. Wu, *Inorg. Chem.*, 2019, **58**, 8943–8947.
51 V. V. Atuchin, S. V. Adichtchev, B. G. Bazarov, Zh. G. Bazarova, T. A. Gavrilova, V. G. Grossman, V. G. Kesler, G. S. Meng, Z. S. Lin and N. V. Surovtsev, *Mater. Res. Bull.*, 2013, **48**, 929–934.
52 W. Liu, X. Liu, X. Meng, C. Li, M. Sun, Z. Lin and J. Yao, *J. Alloys Compd.*, 2022, **902**, 163832.
53 J. Zhou and R. Li, *J. Solid State Chem.*, 2021, **304**, 122630.
54 J. Liu, Y. Chen, M. Sun, W. Liu, X. Meng and J. Yao, *Dalton Trans.*, 2023, **52**, 10109–10114.
55 W. Li, Z. Hu, Y. Ding, Y. Zhu, Q. Jing and L. Liu, *Inorg. Chem.*, 2024, **64**, 371–379.
56 A. B. Kuznetsov, D. M. Ezhov, K. A. Kokh, N. G. Kononova, V. S. Shevchenko, B. Uralbekov, A. Bolatov, V. A. Svetlichnyi, I. N. Lapin, E. A. Simonova and A. E. Kokh, *J. Cryst. Growth*, 2019, **519**, 54–59.
57 V. V. Atuchin, A. K. Subanakov, A. S. Aleksandrovsky, B. G. Bazarov, J. G. Bazarova, S. G. Dorzhieva, T. A. Gavrilova, A. S. Krylov, M. S. Molokeev, A. S. Oreshonkov, A. M. Pugachev, Y. L. Tushinova and A. P. Yelisseyev, *Adv. Powder Technol.*, 2017, **28**, 1309–1315.
58 Z. Xie, Y. Wang, S. Cheng, G. Han, Z. Yang and S. Pan, *Sci. China Mater.*, 2019, **62**, 1151–1161.
59 M. Mutailipu, Z. Xie, X. Su, M. Zhang, Y. Wang, Z. Yang, M. R. S. A. Janjua and S. Pan, *J. Am. Chem. Soc.*, 2017, **139**, 18397–18405.
60 W. Liu, X. Liu, J. Shen, Y. Li, H. Song, J. Feng, Z. Lin and G. Zhang, *Dalton Trans.*, 2020, **49**, 9355–9361.
61 S. J. Yu, X. Y. Gu, T. T. Deng, J. H. Huang, J. W. Cheng and G. Y. Yang, *Inorg. Chem.*, 2017, **56**, 12695–12698.
62 (*a*) CCDC 2475240: Experimental Crystal Structure Determination, 2025, DOI: 10.5517/ccdc.csd.cc2p2pgy; (*b*) CCDC 2475241: Experimental Crystal Structure Determination, 2025, DOI: 10.5517/ccdc.csd.cc2p2phz; (*c*) CCDC 2475242: Experimental Crystal Structure Determination, 2025, DOI: 10.5517/ccdc.csd.cc2p2pj0; (*d*) CCDC 2475243: Experimental Crystal Structure Determination, 2025, DOI: 10.5517/ccdc.csd.cc2p2pk1; (*e*) CCDC 2475244: Experimental Crystal Structure Determination, 2025, DOI: 10.5517/ccdc.csd.cc2p2pl2; (*f*) CCDC 2475245: Experimental Crystal Structure Determination, 2025, DOI: 10.5517/ccdc.csd.cc2p2pm3; (*g*) CCDC 2475246: Experimental Crystal Structure Determination, 2025, DOI: 10.5517/ccdc.csd.cc2p2pn4; (*h*) CCDC 2475247: Experimental Crystal Structure Determination, 2025, DOI: 10.5517/ccdc.csd.cc2p2pp5.